Single and Double Null Equilibria in the SMART Tokamak

S. J. Doyle[1,2], A. Mancini[1,2], M. Agredano-Torres[3,2], J. L. Garcia-Sanchez[4,2], J. Segado-Fernandez[2], J. Ayllon-Guerola[5,2], M. Garcia-Munoz[1,2], E. Viezzer[1,2], and J. Garcia-Lopez[1,2]

[1]Dept. of Atomic, Molecular and Nuclear Physics, University of Seville, Seville, Spain

[2]Centro Nacional de Aceleradores, (U. Seville, CSIC, J. de Andalusia), Seville, Spain

[3]Max-Planck-Institute for Plasma Physics, 17491 Greifswald, Germany

[4]Skylife Engineering S.L., 41092, Seville, Spain

[5]Dept. of Mechanical Engineering and Manufacturing, University of Seville, Seville, Spain

[1]E-mail: Scott.Doyle@Physics.org

August 16, 2021

Abstract

The *SMall Aspect Ratio Tokamak* (SMART) device is a novel, compact (R_{geo} = 0.42 m, a = 0.22 m, $A \geq 1.75$) spherical tokamak, currently under development at the University of Seville. The SMART device is being developed over 3 phases, with target on-axis toroidal magnetic fields between $0.1 \leq B_\phi \leq 1.0$ T, and target plasma currents of between $35 \leq I_p \leq 500$ kA; with phases 2 and 3 enabling access to a wide range of elongations ($\kappa \leq 2.25$) and triangularities ($-0.50 \leq \delta \leq 0.50$). SMART employs four internal divertor coils with two internal and two external poloidal field coils, enabling operation in lower-single, upper-single and double-null configurations. This work examines phase 3 of the SMART device, presenting a prospective L-mode discharge scenario without external heating, before examining five highly-shaped equilibria, including: two double null triangular configurations, two single null triangular configurations and a baseline double null configuration. All equilibria are obtained via an axisymmetric Grad-Shafranov force balance solver (Fiesta), in combination with a circuit equation rigid current displacement model (RZIp) to obtain time-resolved vessel and plasma currents.

Keywords: *Spherical Tokamak, Equilibrium, Triangularity, Divertor, SMART*

1 Introduction

Magnetically confined plasmas exist in state of balance between their internal thermal pressure, their self-generated magnetic forces, and any externally applied magnetic forces[1,2]. Within the Grad-Shafranov model, the plasma is confined to an infinite set of nested flux surfaces, where the last closed flux surface (LCFS) defines the shape of the poloidal cross-section[3]. The plasma is then bounded either physically (limited plasma) or magnetically (diverted plasma), where the LCFS exhibits one or more poloidal magnetic nulls, of which there are numerous geometries[4–7], enabling a controlled exhaust from the plasma column. The precise shape of the LCFS, and how it is diverted, are fundamental design aspects and impact all discharge parameters[8–10].

The role of plasma shaping on discharge performance is a topic of much recent interest, in particular how the equilibrium shape affects radial transport and edge transport boundary[10,11]. Pioneering work performed at TCV[8] first demonstrated that negatively triangular plasma cross-sections significantly impact the energy confinement time, electron heat transport[10], core stability[12], and edge stability[9,13,14] in L and H-mode plasmas. More recently, negatively triangular L-mode plasmas at DIII-D[15] have been demonstrated to achieve *'H-mode-like'* confinement characteristics in the absence of an edge pressure pedestal, indicating the potential for commercial L-mode reactors[16]. The choice of divertor geometry further alters the magnetic topology at the LCFS boundary[17–19], affecting edge plasma properties, internal transport, and confinement.

While much theoretical and experimental work has been performed examining the impacts of plasma shaping and divertor configurations in traditional high aspect ratio tokamaks, their effects on low aspect ratio spherical tokamaks (ST) is still largely unknown. In the three decades since their conception with the START device[20–22] numerous ST have been designed and operated, including but not limited to: MAST[23,24], NSTX[25], Globus-M[26] & Globus-M2[27], QUEST[28,29], LTX[30,31], ST40[32,33], and VEST[34,35]. The aggregated findings from these and other STs demonstrate; high bootstrap current fractions[21,36], enhanced plasma β, and improved stability to pressure driven[37] and particle-driven[38,39] instabilities as compared to traditional high-aspect ratio designs. While these results are encouraging, there still remain open questions regarding how plasma transport and stability are affected in highly shaped, low-aspect ratio plasmas.

To address this, a novel compact spherical tokamak named the *SMall Aspect Ratio Tokamak* (SMART) is being designed at the University of Seville to serve as a low-cost, versatile, and educational fusion research device[40–42]. Development of the SMART device will proceed in three phases, with the third and final phase providing significant discharge flexibility, being capable of achieving low aspect ratio ($A \geq 1.67$), highly elongated ($\kappa \leq 2.32$), highly triangular ($-0.50 \leq \delta \leq +0.50$)

equilibrium geometries and operating in upper single null (USN), lower single null (LSN), and double-null configurations.

This work focuses on the third and final phase SMART development, presenting conservative predictions outlining the degree of achievable plasma shaping, specifically the capability for single and double null configurations, and contextualizing the expected capabilities of the finished device within the field. A brief outline of the SMART device, and the numerical methods employed in this work, are given in sections 2 and 3. An overview of key parameters through the SMART development pipeline are presented alongside a typical phase 3 discharge scenario in 4, before examining five prospective shaped equilibria in section 5, followed by a comparison of key operating parameters to other similar operating devices.

2 SMART Device Overview

An overview of the SMART device is shown in figure 1 (a), illustrating the vacuum vessel in grey, toroidal field (TF) coils in orange, poloidal field (PF) coils and divertor (Div) coils in yellow, and the central solenoid (Sol) in red. Figure 1 (b) shows the associated simulation domain employed in this work, corresponding to an axis-symmetric 2D cross-section of the torus, and is discussed in more detail with regards to the numerical model in section 3.

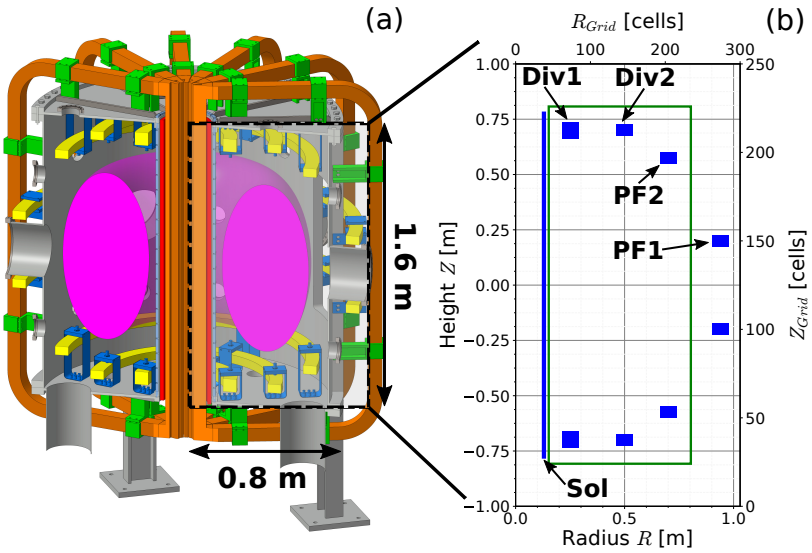

Figure 1: Overview of the SMART device showing (a) a 3D cutaway of the vessel and coil geometry, and (b) the 2D axisymmetric mesh employed in this work. The vacuum vessel is shown in grey, toroidal field coils in orange, poloidal field coils and divertor coils in yellow, solenoid in red and supports in blue and green.

A brief overview of the SMART device is presented here, for full details see Refs.[40–42]. SMART consists of a 0.8 m radius by 1.6 m height stainless steel (AISI 316 L) vacuum vessel, with a total internal volume of 3.1 m^3, of which approximately 1.8 m^3 is utilizable for the plasma column. The vacuum system comprises four pumps including two dry 80 m^3h^{-1} pumps and two turbomolecular

2300 ls^{-1} pumps, capable of achieving a vacuum of 1.33×10^{-6} Pa (10^{-8} Torr). Thermal protection is provided by carbon tiles affixed to the inboard wall, denoted in pale blue, and steel jackets fitted to the inboard coils (not shown), providing protection against unexpected plasma displacements or disruptions in lieu of dedicated limiters for plasma boundary control.

The toroidal field is provided by a set of twelve 4 turn copper TF coils, capable of maintaining up to 1 T on-axis ($R = 0.42$ m) for 1000 ms, requiring a central stack current of 2.1 MA, or 43.75 kA/turn. Thermal modelling[42] predicts TF coil temperatures remain below 80 $^\circ$ C without cooling - adhearing to the 100 $^\circ$ C operating limit imposed by the epoxy insulation[43]. Plasma shaping and control is facilitated by two pairs of PF coils and two further pairs of Div coils enabling operation in both upper and lower single-null configurations and double-null configurations, with phase 3 PF and Div coil power supplies capable of supplying up to $\pm$ 8 kA at $\leq$ 300 A/ms. The inboard Div1 coil set comprises a larger construction, serving as the primary divertor coil, while the outboard Div2 coil set is constructed in the same fashion as the PF coils, providing active vertical control.

Plasma startup and ohmic heating is provided by a central 1.55 m tall, 240 turn, 0.15 m outer radius copper solenoid, situated surrounding the central TF coil stack. The phase 3 solenoid power supply will facilitate a maximum current swing of $\pm$ 18 kA ($\leq$ 375 A/ms), providing a magnetic flux variation of 0.40 Wb. Plasma breakdown may be assisted via a pre-ionisation step employing 6 kW (2.45 GHz or 7.5 GHz) of microwave heating. From phase 3, up to 200 kW of Electron Cyclotron Resonance Heating (ECRH) will also be made available. The installation of a Neutral Beam Injector (NBI) from phase 2 onwards introduces a further 600 kW of plasma heating. The work presented here represents L-mode operation in the absence of external heating, future works will address SMART operation in H-mode.

The SMART device will proceed through three developmental phases, detailed in table 1, with each phase affording a significant increase in plasma current, pulse duration, and achievable plasma shaping[40–42].

Parameter	Phase 1	Phase 2	Phase 3
R_{geo} [m]	$\geq$ 0.4	$\geq$ 0.4	$\geq$ 0.4
a [m]	$\geq$ 0.2	$\geq$ 0.2	$\geq$ 0.2
n_e [m^{-3}]	1×10^{19}	5×10^{19}	1.0×10^{20}
T_e [eV]	100	250	750
T_i [eV]	30	100	400
A [-]	$\geq$ 1.85	$\geq$ 1.85	$\geq$ 1.70
κ [-]	$\leq$ 1.95	$\leq$ 2.00	$\leq$ 2.25
δ [-]	$\pm$0.40	$\pm$0.50	$\pm$0.50
B_ϕ [T]	0.1	0.3	1.0
I_p [kA]	40	100	400
τ_{ft} [ms]	80	100	500
β_n [-]	$\leq$ 2.8	$\leq$ 4.2	$\leq$ 5.0
P_{ECRH} [kW]	6 (2.45 GHz)	6 (7.5 GHz)	200
P_{NBI} [kW]	-	$\leq$ 600	600

Table 1: Target operational parameters of the SMART device for developmental phases 1 - 3. All parameters are determined within Fiesta, excepting P_{ECRH} and P_{NBI}, which are prescribed engineering targets, and electron density n_e and temperature T_e, which are provided by the ASTRA transport code[44,45]. The temperatures and densities provided for phases 2 and 3 are representative of L-mode operation without external heating.

Phase 1 of SMART will achieve first plasma (in hydrogen) and serve as a proof-of-concept for the design, while enabling testing and training in mission operations and key diagnostics. Phase 2 sees the introduction and step-wise implementation of the NBI heating systems ($200 \leq P_{NBI} \leq 600$ kW), vertical control and feedback system, and moderate enhancements to the toroidal field strength, plasma current, pulse duration, and plasma shaping capabilities. Phase 3 represents significant improvements to the achievable toroidal field ($B_\phi = 1.0$ T), plasma density ($n_e = 1.0 \times 10^{20}$ m^{-3}), flat-top current ($I_p \leq 400$ kA), temperature ($T_e = 750$ eV), and heating ($P_{NBI} = 600$ kW), bringing SMART's capabilities in-line with other contemporaneous spherical devices.

3 Numerical Model

Discharge configurations, breakdown thresholds, and current evolution were modelled employing the *Fiesta* code environment[46–48]. The numerical scheme consists of a linear current density model (based upon TOPEOL[49]), a free-boundary axisymetric equilibrium solver, EFIT[50], and a rigid current displacement circuit equation model, RZIp[48,51–53]. A brief overview of the numerical model is given here,

for full details see Ref. 40. All simulations are performed on a 2D 300 $\times$ 251 ($R \times Z$) rectilinear grid, shown previously in figure 1 (b). The vessel walls, PF and Div coil sets, and central solenoid are modelled as toroidal current carrying filaments. As the model employs an axisymmetric boundary TF coils are not included within the grid, instead the toroidal magnetic field B_ϕ is scaled relative to the central rod current via: $B_\phi(R) = \mu_0 I_{rod}/2\pi R$, where I_{rod} is the sum total of the TF coil currents.

Equilibria are computed via the EFIT model, where the Grad-Shafranov force balance equation can be solved in a 'forward' or 'inverse' manner. In the 'forward' manner, fixed boundary conditions are set by the instantaneous Sol, PF, and Div coil currents in I_{coils}, the current density profile $J(\mathbf{R})$, and the toroidal magnetic field at a defined time τ. As the PF and Div coil current configuration is pre-specified. The 'inverse' method, as employed in this work, utilizes the same pre-computed p', ff', and $J(\mathbf{R})$ profiles at time τ, but fits the equilibrium $\psi(R, Z)$ to a prescribed set of target plasma shaping parameters, R_{geo}, Z_{geo}, a, κ and δ. The PF and Div coil current configuration required to achieve the desired equilibrium shape is then provided as a solution rather than an input, while still adhering to the prescribed current density profile. In both cases the prescribed current density profile is scaled relative to p' and ff', employing the flat-top plasma current to determine the on-axis current density j_0.

The current density profile and associated pressure p' and poloidal current ff' profiles (differentiated with respect to ψ) are scaled relative to the poloidal beta β_θ via equations 1 and 2, respectively.

$$p' = \left(\frac{1}{R_{geo}}\right) \beta_\theta (1 - \psi_n^m)^n \tag{1}$$

$$ff' = \mu_0 R_{geo} (1 - \beta_\theta)(1 - \psi_n^m)^n \tag{2}$$

where ψ_n is the normalised poloidal flux, defined as:

$$\psi_n = \frac{\psi - \psi_0}{\psi_b - \psi_0} \qquad \text{and} \qquad 0 \leq \psi_n \leq 1 \tag{3}$$

Here, R_{geo} is the geometric axis, ψ_0 is the poloidal flux on-axis (at R_{geo}), and ψ_b is the poloidal flux at the last closed flux surface (LCFS) boundary, implicitly setting p' and ff' to zero at the LCFS. The variables m and n enable non-linear scaling of the p' and ff' profiles, however a linear scaling model ($m = n = 1$) was employed in this work. The poloidal beta β_θ, defined as the ratio between the thermal and poloidal magnetic pressures, is computed via equation 4, where parameters are as previously indicated:

$$\beta_\theta = 3\mu_0 e \frac{n_e \kappa (T_e + T_i)}{(\mu_0 I_p / 2\pi a)^2} \tag{4}$$

Here, the thermal pressure term is scaled relative to the on-axis plasma density n_e, electron temperature T_e, ion temperature T_i, and plasma elongation κ, all shown in table 1. The prospective discharge configurations and equilibria presented in this work utilize ohmically heated L-mode on-axis density and temperatures obtained via ASTRA [44,45] transport simulations, while the elongation and minor radius match efit target shaping parameters. Within ASTRA, a Gyrobohm model was employed [54], where the electron χ_e, ion χ_i transport coefficients, and diffusion coefficient D were allowed to vary over the minor radius, assuming a pure ion transport gradient (ITG) dominated plasma such that $\chi_e = 2 * \chi_i$, and $D \propto \chi_e$.

Temporally resolved currents and voltages are obtained via RZIp, a rigid circuit displacement model [48,51–53]. RZIp computes time-resolved currents and voltages based upon a matrix application of Ohm's law, accounting for material resistivities, self-inductances, and the mutual inductance between all coil and vessel filaments. To achieve this, vessel, coil, and solenoid filaments are each assigned an equivalent resistance and inductance based upon their material coefficients and relative geometry. The plasma column is included as a single toroidal filament possessing a constant poloidal cross-section and current density profile, as provided by EFIT. While the filament area is fixed, the radial and axial position of the plasma column may change in response to $\mathbf{J} \times \mathbf{B}$ forces, responding to changes in coil or vessel currents.

The coils are first current driven, where the coil current waveforms (see figure 2 (a)) are employed to calculate the coil filament voltages, vacuum vessel filament voltages, plasma voltage, and plasma current. Next, the plasma voltage and current profiles are set to zero for all times prior to breakdown. Finally, the coils are voltage driven, employing the previously calculated coil filament voltages, vacuum vessel filament voltages, and modified plasma voltage to re-calculate the plasma current and vessel eddy currents. This treatment ensures that the plasma and vessel eddy currents include effects from all coil and vessel filaments, and are temporally consistent with the computed plasma breakdown.

4 Discharge Scenarios

The Sol, PF, and Div coil current configurations for a prospective phase 3 discharge are presented in figure 2 (a), with the associated plasma current and net vessel eddy current in figure 2 (b), and the induced loop voltage V_{loop} in figure 2 (c).

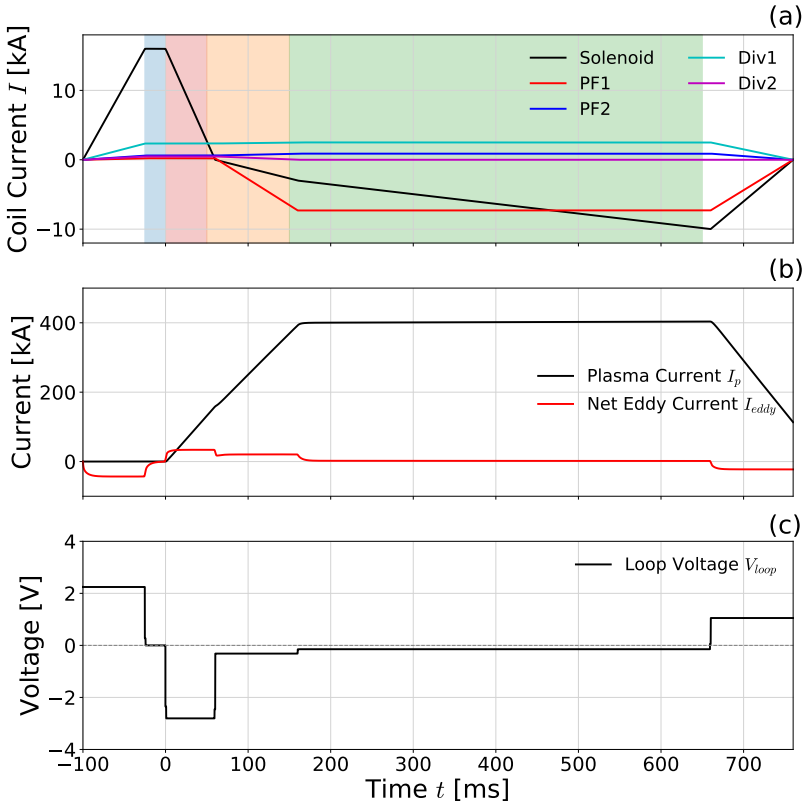

Figure 2: Prospective SMART phase 3 discharge scenario, showing (a) Sol, PF and Div coil current waveforms, (b) the time-resolved plasma current, and (c) the induced loop voltage V_{loop}. Operational stages consist of a null-field stage (denoted blue), plasma breakdown (denoted red), transition stage (denoted orange), and plasma current flat-top (denoted green). Operating Conditions: $I_p = 400$ kA, $B_\phi = 1.0$ T, $\tau_{ft} = 500$ ms.

The discharge procedure shown in figure 2 (a), consists of four stages: a null-field stage between $t = -25$ ms to $t = 0$ ms, denoted blue; a breakdown stage between $t = 0$ ms to $t = 50$ ms, denoted red; a transition stage between $t = 50$ ms to $t = 150$ ms, denoted orange; and the flat-top discharge stage from $t = 150$ ms to $t = 650$ ms, denoted green. Examining each of these stages it can be seen that, prior to breakdown, the Sol, PF, and Div coils are ramped into their null-field configuration between $t = -100$ ms to $t = -25$ ms. This configuration is maintained for 25 ms allowing suitable time for vessel eddy currents to decay and for the on-axis poloidal magnetic field $\mathbf{B}_\theta$ to reach a minimum of 1.6 G. The pulse initiates at $t = 0$ ms with a 15 kA (300 A/ms) solenoid ramp inducing a maximum loop voltage of $V_{loop} = 3.1$ V as shown in figure 2 (c). This ramp is sustained for 50 ms, facilitating ohmic breakdown, with the discharge reaching the coulomb phase (electron-ion collisions exceed electron-neutral collisions) within 6 ms for a pre-fill pressure of 0.05 mTorr. Full details of the null-field optimisation process, including an explicit computation of plasma breakdown parameters, can be found in Ref. 40. The solenoid ramp also induces eddy currents within the vacuum vessel, most predominantly on the inboard side, with net vessel eddy currents reaching a maximum of $I_{eddy} = 35$ kA, as shown in figure 2 (b). While these vessel eddy currents do initially grow faster than the plasma current, they are quickly overtaken following breakdown, with the plasma current exceeding the net

vessel eddy current by $\approx$ $t = 15$ ms.

Following breakdown the plasma current grows at $\approx$ 3.5 MA/s, reaching 175 kA by the start of the transition stage at $t = 50$ ms, as shown in figure 2 (b). Simultaniously, the PF and Div coils swing into their discharge configuration and the solenoid current ramp is reduced to -37.5 A/ms, maintaining a plasma current growth of 2.25 MA/s for a further 100 ms. By $t = 150$ ms the plasma current has reached a flat-top current of 400 kA, and the plasma equilibrium possesses the desired shape, to be presented in section 5. A final shallow tertiary solenoid current ramp between $t = 150$ ms to $t = 650$ ms (14.5 A/ms) drives a sustaining loop voltage of 0.13 V and maintains the 400 kA flat-top current against internal resistive losses and external inductive losses to the vessel walls, both captured within the RZIp model. The precise configuration of the PF and Div coil currents varies within the flat-top phase depending upon the target equilibrium shape; however, the optimised null-field and start-up procedure (denoted blue and red) remain similar for all phase 3 discharges.

5 SMART Phase 3 Null Configurations and Shaping Capabilities

Representative SMART phase 3 equilibria illustrating the extrema in positive and negative triangularity for both double null and upper or lower single null divertor configurations are shown in figures 3 (a-e). All equilibria are computed at time $t = 150$ ms employing discharge parameters as shown in table 1, and respect the current and voltage limitations of the phase 3 power supplies[42], and the thermal and structural limitations of the coils and vacuum vessel[41]. Note also that the inverse of 3 (a) and (e), i.e. upper single null $-\delta$ and lower single null $+\delta$, may also be achieved but are omitted here for brevity.

Figure 3 (c) provides a baseline equilibrium for comparison, and represents the shape achieved for a 'standard' phase 3 discharge shown in figure 2 (a). The baseline configuration maximises the elongation ($\kappa = 2.32$) for a double-null, moderate aspect ratio ($A = 1.88$), positively triangular ($\delta = +0.18$), 0.9 m^3 plasma column, utilizing 50% of the usable vessel volume.

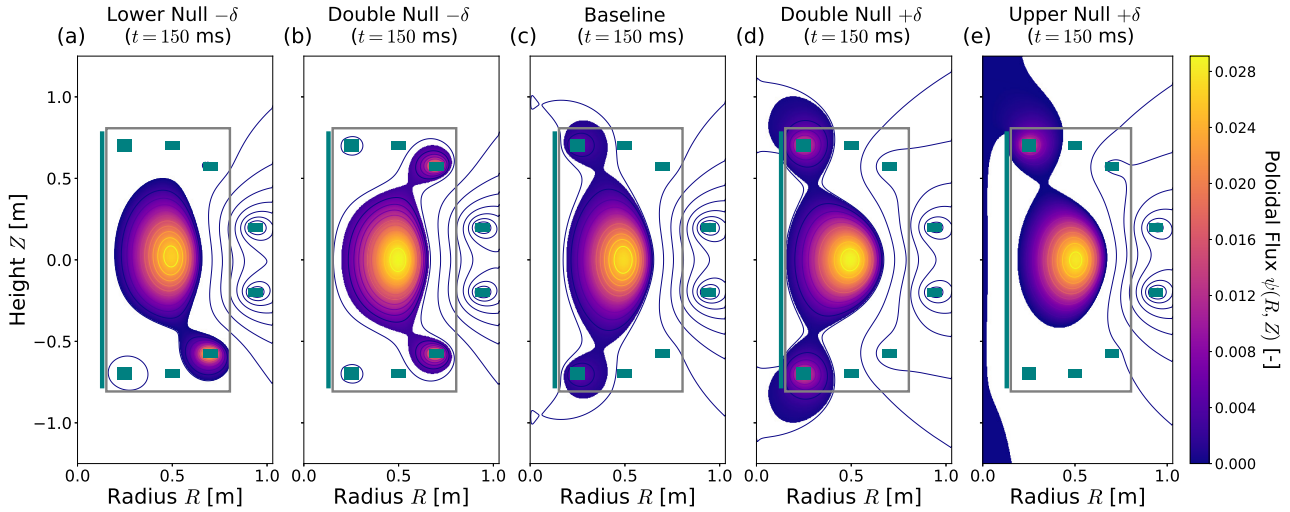

Figure 3: Phase 3 discharge equilibria, (a) lower single null negative triangularity ($\delta = -0.30$, $\kappa = 2.02$, $A = 1.94$), (b) double null negative triangularity ($\delta = -0.50$, $\kappa = 1.98$, $A = 1.93$), (c) baseline elongated ($\delta = +0.18$, $\kappa = 2.32$, $A = 1.88$), (d) double null positive triangularity ($\delta = +0.42$, $\kappa = 1.75$, $A = 1.67$), (d) upper single null positive triangularity ($\delta = +0.25$, $\kappa = 1.81$, $A = 1.84$). All equilibria are computed during the plasma current flat-top at $t = 150$ ms (see figure 2). The vacuum vessel is denoted in grey, while coils and solenoid are shown in teal. Operating Conditions: $I_p = 400$ kA, $B_\phi = 1.0$ T, $\tau_{ft} = 500$ ms.

Figures 3 (b) and (d) exhibit the double null negative triangularity ($\delta = -0.50$) and double null positive triangularity configurations ($\delta = +0.42$), respectively. Both cases exhibit reduced elongations as compared to the baseline case, where $\kappa = 1.75$ for the $+\delta$ case and $\kappa = 1.98$ for the $-\delta$ case. This effect is most pronounced for the $+\delta$ configuration, where increased Div1 coil currents are required to maintain the inboard LCFS from the inboard wall, resulting in a shorter and 'broader' poloidal cross-section. While limiting the achievable $+\delta$ elongation, this has the beneficial effect of maximising the minor radius a, and resulting in a minimised aspect ratio of $A = 1.67$, as compared to $A \approx 1.9$ for the baseline and $-\delta$ configurations. The double null baseline and $+\delta$ configurations exhibit safety factors of $q_{95} = 6.6$ and $q_{95} = 6.5$, respectively, as compared to $q_{95} = 4.7$ for the double null $-\delta$ configuration. This discrepancy is explained via noting that a larger proportion of the plasma column is held closer to the high-field side for highly elongated or positively triangular configurations, resulting in a higher average B_ϕ 'seen' along any particular closed flux surface.

The associated shaped single null equilibria are shown in figures 3 (a) and (e), illustrating the lower single null negative triangularity ($\delta = -0.30$) and upper single null positive triangularity ($\delta = +0.25$) configurations, respectively. As noted earlier, either combination of upper or lower single null and positive or negative triangularity can be achieved, with only two cases being presented here for brevity. Operating with a single null point exchanges a reduction in the achievable triangularity for an increase in elongation, achieving $\kappa = 2.02$ for the $-\delta$ case and $\kappa = 1.81$ for the $+\delta$ case, with aspect ratios of $A = 1.94$ and $A = 1.84$, respectively. Both shapes exhibit edge safety factors lower than the baseline configuration, the effect being most pronounced for the $-\delta$ configuration, where $q_{95} = 4.8$, as compared

to $q_{95} = 5.2$ for the $+\delta$ configuration.

The normalised plasma beta ranges between $4.0 \leq \beta_n \leq 4.8$, with the single null configurations exhibiting the lowest values. Similar trends are observed for the poloidal and toroidal plasma betas, ranging $1.1 \leq \beta_{pol} \leq 1.4$ and $7.0\% \leq \beta_{tor} \leq 8.1\%$, respectively. These values, particularly β_n and β_{pol}, compare well to similar devices, notably NSTX[55]: $\beta_{tor} \leq 35\%$, $\beta_n \leq 6.4$, $\beta_{pol} \leq 1.4$, and MAST[23]: $\beta_{tor} \leq 16\%$, $\beta_n \leq 5.3$, $\beta_{pol} \leq 1.7$. The reduced β_{tor} range exhibited by SMART arises primaily due to operation in L-mode, while the values stated for NSTX and MAST represent H-mode operation. When operated employing NBI and ECR heating it is expected that SMART will achieve significantly higher toroidal betas.

It is worth noting that the single null configurations offer significantly more independent control over the upper and lower triangularities, which are typically axially symmetric for double null configurations. This may be achieved through preferentially increasing the elongation on the non-null side, e.g. the $+Z$ region for 3 (a) and visa-versa, while maintaining the elongation on the null side. Such control is primarily afforded through variation of the non-null divertor coil current, but may also be influenced through careful alteration of the equilibrium solenoid current, where more negative equilibrium solenoid currents enforce a sharper 'corner' at the non-null side. In general this implies that more negative equilibrium solenoid currents are desirable for single null triangular operation, as opposed to double null triangular configurations where an equilibrium solenoid current close to zero is preferred. In this manner, single null configurations enable the discrete analysis of a wider range of vertically asymmetric triangular plasmas compared to double null configurations.

In addition, SMART offers the capability to rapidly switch between single null configurations within a single discharge. Transitioning from a LSN to USN configuration without significantly altering the equilibrium shape (A, κ, δ) could be achieved in ≈ 25 ms, being primarily limited by the PF or Div coil power supply considerations. In practice, this is achieved through symmetrically reversing the coil currents in the upper and lower PF and Div coil sets, with the inboard null-forming divertor coils (Div1) experiencing the largest change in current. The switching timescale was found to be limited by the null-forming inboard divertor coil (Div1) current rather than the degree of shaping, being primarily related to the PF coil currents. As such, the $+\delta$ configurations exhibit slower switching timescales due to the larger separation between the inboard divertor coil and the more radially extended plasma column. Ramping the PF and Div coil currents over such short timescales is expected to induce currents in both the vacuum vessel and plasma column. For the case of 'symmetric' null transitions, where the equilibrium shape is maintained, the net effect on the plasma current is likely to be quite small, however opposing vessel eddy currents would be induced on the top and bottom of the vacuum

vessel.

For 'asymmetric' null transitions, where both the null and the equilibrium shape are altered, this up-down coil symmetry is broken due to the upper and lower coils requiring different currents for each shape, and hence a net induced plasma current is expected. Whether the coil ramps enhance or suppress the plasma current is situationally dependent, for example transitioning between a $-\delta$ LSN to a $+\delta$ USN (figures 3(a) and (e)) would involve positive upper and lower Div coil current ramps, inducing a counter-current. To address this, the solenoid current would be ramped (with a negative gradient) during the transition to counteract the loss in plasma current, similar to that already performed during the transition phase in figure 2 (a). In fact, the switching timescale of 25 ms was chosen such that the maximum required PF and Div coil current gradients are strictly below those employed in the figure 2 transition phase, adhering to their respective power supply limitations. How the MHD stability is affected during such a null transition is unfortunately beyond the scope of this paper.

An examination of key operating and shaping parameters is presented in figure 4, for a range of spherical devices, namely NSTX[25,55,56], MAST[23,57], GLOBUS-M2[27,58], VEST[34,59–61], and QUEST[28,29,62]. Here, all parameters represent their maximum achievable values (not necessarily simultaneously) and are normalised between $0 - 1$, with 1 representing the maximum between all presented machines, for ease of comparison. Please note that while VEST can in principle achieve negative triangular equilibria this capability has not yet been assessed. Data pertaining to the capabilities of GLOBUS-M2, NSTX, and MAST with respect to achievable negative triangularities was not available for comparison.

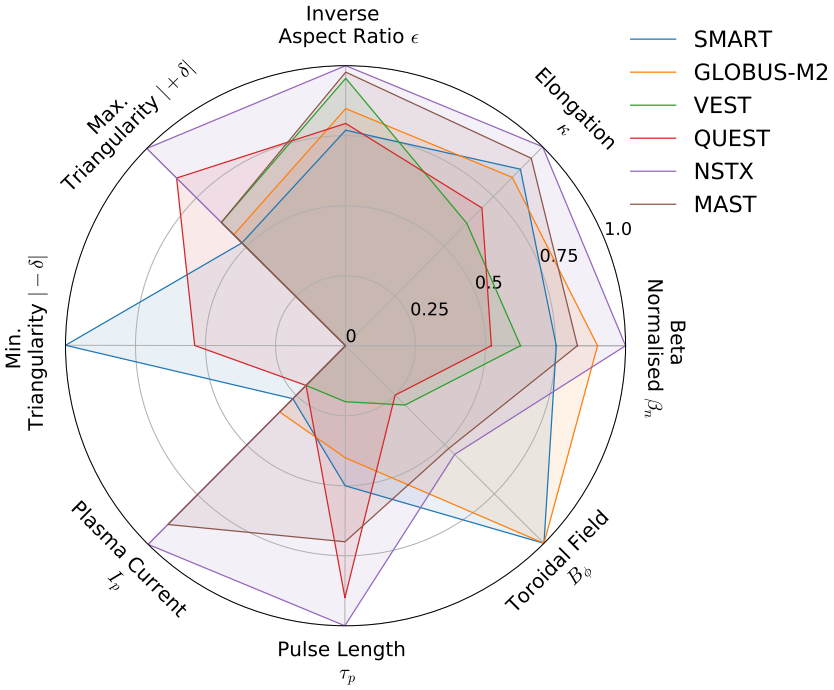

Figure 4: A comparison of maximum achievable key operating and shaping parameters between SMART phase 3, NSTX[25,55,56], MAST[23,57], GLOBUS-M2[27,58], VEST[34,59–61] and QUEST[28,29,62]. All parameters are normalised between $0 - 1$ for ease of comparison. SMART phase 3 shaping parameters are obtained from equilibria presented in figure 2.

As can be seen from figure 4, SMART phase 3 generally compares well to other small-to-mid sized devices, particularly with respect to its high toroidal field, while achieving moderate plasma currents and pulse lengths as compared to the larger machines. With regards to shaping parameters, SMART enables access to a wide range of low aspect ratio ($A \geq 1.67$), highly-elongated ($\kappa \leq 2.32$) plasma shaping configurations, with double null configurations achieving the lowest aspect ratios. In particular SMART offers the unique capability to achieve significantly negative triangular configurations ($\delta \geq -0.50$) in a spherical geometry, noting that this comes at the cost of a slightly reduced range of positive triangular configurations. SMART's discharge flexibility is further enhanced through access to single and double null configurations. Future access to exotic null configurations (e.g. snowflakes) is technically feasible, however is not currently envisaged.

In summary, SMART phase 3 offers a wide range of discharge scenarios and equilibrium shaping configurations, comparing well to similar sized spherical devices. Within the field, SMART will uniquely enable access to a wide range of negatively triangular configurations, hitherto not studied within spherical geometries. The wide range of achievable equilibria, demonstrated in figures 3 (a-e), will enable SMART to contribute in the areas of: heat transport, energy confinement, edge plasma flows, and MHD stability in spherical tokamaks. Further, construction, characterisation, and upgrade of the SMART device through phases 1 - 3 will provide a testing ground for novel plasma diagnostics and facilitate the training of the next generation of fusion physicists and engineers.

6 Conclusions

Prospective L-mode ohmic discharge scenarios and shaped plasma equilibria for phase 3 of the *SMall Aspect Ratio Tokamak* (SMART) device have been simulated employing a 2D axisymmetric free boundary model (Fiesta). An overview of SMART phases 1-3 was presented, including the details of a prospective phase 3 discharge scenario. Five phase 3 target equilibria were presented, including: a baseline elongated configuration ($A = 1.88$, $\kappa = 2.32$), a pair of double null configurations ($-0.50 \leq \delta \leq +0.42$), and a pair of single null configurations ($-0.30 \leq \delta \leq +0.25$). Predictive plasma betas in the range $4.0 \leq \beta_n \leq 4.8$ were achieved, with plasma shaping and discharge parameters comparing well to other spherical devices. Single null configurations were found to exchange reduced triangularity for increased elongation and discharge flexibility, more readily enabling independent modulation of upper and lower triangularities. The capability to maintain highly flexible single and double null negatively triangular plasmas within a spherical geometry, in combination with both NBI and ECR heating, ensures that SMART phase 3 is well positioned to produce significant contributions to the field in the areas of heat transport, edge physics, and MHD stability in low aspect ratio plasmas.

7 Acknowledgements

The authors would like to thank the VEST team for their technical and engineering support. This work received funding from the Fondo Europeo de Desarollo Regional (FEDER) by the European Commission under grant agreement numbers IE17-5670 and US-15570. In addition support from the European Research Council (ERC) under the European Union's Horizon 2020 research and innovation programme (grant agreement No. 805162) is gratefully acknowledged.

8 References

[1] H. Grad and H. Rubin, "Hydromagnetic equilibria and force-free fields," *Journal of Nuclear Energy (1954)*, vol. 7, no. 3-4, pp. 284–285, 1958.

[2] V. Shafranov, "On Magnetohydrodynamical Equilibrium Configurations," *Soviet Journal of Experimental and Theoretical Physics*, vol. 6, no. 3, p. 545, 1958.

[3] G. O. Ludwig, "Plasma Physics and Controlled Fusion Direct variational solutions of the tokamak equilibrium problem Direct variational solutions of the tokamak equilibrium problem," *Plasma Physics and Controlled Fusion*, vol. 39, p. 2021, 1997.

[4] T. W. Petrie, S. L. Allen, M. E. Fenstermacher, R. J. Groebner, C. T. Holcomb, *et al.*, "Application of the radiating

divertor approach to innovative tokamak divertor concepts," *Journal of Nuclear Materials*, vol. 463, pp. 1225–1228, 2015.

[5] H. Y. Guo, D. N. Hill, A. W. Leonard, S. L. Allen, P. C. Stangeby, *et al.*, "Developing and validating advanced divertor solutions on DIII-D for next-step fusion devices," *Nuclear Fusion*, vol. 56, no. 12, p. 126010, 2016.

[6] V. A. Soukhanovskii, R. E. Bell, A. Diallo, S. Gerhardt, S. Kaye, *et al.*, "Snowflake divertor configuration studies in National Spherical Torus Experiment," *Physics of Plasmas*, vol. 19, no. 8, p. 082504, 2012.

[7] D. D. Ryutov, "Geometrical properties of a "snowflake" divertor," *Physics of Plasmas*, vol. 14, no. 6, p. 064502, 2007.

[8] Y. Camenen, A. Pochelon, R. Behn, A. Bottino, A. Bortolon, *et al.*, "Impact of plasma triangularity and collisionality on electron heat transport in TCV L-mode plasmas," *Nuclear Fusion*, vol. 47, no. 7, pp. 510–516, 2007.

[9] M. Fontana, L. Porte, S. Coda, and O. Sauter, "The effect of triangularity on fluctuations in a tokamak plasma," *Nuclear Fusion*, vol. 58, no. 2, p. 024002, 2018.

[10] C. T. Holcomb, J. R. Ferron, T. C. Luce, T. W. Petrie, P. A. Politzer, *et al.*, "Optimizing stability, transport, and divertor operation through plasma shaping for steady-state scenario development in DIII-D," *Physics of Plasmas*, vol. 16, no. 5, p. 056116, 2009.

[11] F. Hofmann, O. Sauter, H. Reimerdes, I. Furno, and A. Pochelon, "Experimental and Theoretical Stability Limits of Highly Elongated Tokamak Plasmas," *Phys. Rev. Lett.*, vol. 81, p. 2918, 1998.

[12] D. Testa and A. Fasoli, "The effect of plasma shaping on the damping of low n Alfvén eigenmodes in JET tokamak plasmas," *Nuclear Fusion*, vol. 41, no. 7, pp. 809–812, 2001.

[13] A. Kendl and B. D. Scott, "Flux-surface shaping effects on tokamak edge turbulence and flows," *Physics of Plasmas*, vol. 13, no. 1, pp. 1–9, 2006.

[14] F. Riva, E. Lanti, S. Jolliet, and P. Ricci, "Plasma shaping effects on tokamak scrape-off layer turbulence," *Plasma Physics and Controlled Fusion*, vol. 59, no. 3, p. 035001, 2017.

[15] M. E. Austin, A. Marinoni, M. L. Walker, M. W. Brookman, J. S. Degrassie, *et al.*, "Achievement of Reactor-Relevant Performance in Negative Triangularity Shape in the DIII-D Tokamak," *Physical Review Letters*, vol. 122, no. 11, p. 115001, 2019.

[16] M. Kikuchi, T. Takizuka, S. Medvedev, T. Ando, D. Chen, *et al.*, "L-mode-edge negative triangularity tokamak reactor," *Nuclear Fusion*, vol. 59, no. 5, p. 056017, 2019.

[17] M. Barbarino, A. Leonard, N. N. Asakura, M. Jakubowski, M. Kobayashi, *et al.*, "Summary of the 3rd IAEA technical meeting on divertor concepts," *Nuclear Fusion*, vol. 60, no. 9, p. 097001, 2020.

[18] F. Piras, S. Coda, I. Furno, J. M. Moret, R. A. Pitts, *et al.*, "Snowflake divertor plasmas on TCV," *Plasma Physics and Controlled Fusion*, vol. 51, no. 5, p. 055009, 2009.

[19] P. M. Valanju, M. Kotschenreuther, S. M. Mahajan, and J. Canik, "Super-X divertors and high power density fusion devices," *Physics of Plasmas*, vol. 16, no. 5, p. 056110, 2009.

[20] A. Sykes, R. J. Akers, L. C. Appel, P. G. Carolan, J. W. Connor, *et al.*, "H-mode operation in the start spherical tokamak," *Physical Review Letters*, vol. 84, no. 3, pp. 495–498, 2000.

[21] M. Gryaznevich, R. Akers, P. G. Carolan, T. Erneux, D. Gates, *et al.*, "Achievement of record β in the START spherical tokamak," *Physical Review Letters*, vol. 80, no. 18, pp. 3972–3975, 1998.

[22] A. Sykes, G. W. Crawford, G. Cunningham, N. A. Fawlk, D. H. Goodall, *et al.*, "START spherical tokamak," *Proceedings - Symposium on Fusion Engineering*, vol. 2, pp. 1442–1446, 1995.

[23] B. Lloyd, J. W. Ahn, R. J. Akers, L. C. Appel, E. R. Arends, *et al.*, "Overview of recent experimental results on MAST," *Nuclear Fusion*, vol. 43, no. 12, pp. 1665–1673, 2003.

[24] A. C. Darke, M. Cox, J. R. Habar, J. H. Hay, J. B. Hicks, *et al.*, "The Mega Amp Spherical Tokamak," *Proceedings - Symposium on Fusion Engineering*, vol. 2, pp. 1456–1459, 1995.

[25] S. M. Kaye, M. G. Bell, R. E. Bell, S. Bernabei, J. Bialek, *et al.*, "Progress towards high performance plasmas in the National Spherical Torus Experiment (NSTX)," *Nuclear Fusion*, vol. 45, no. 10, p. S168, 2005.

[26] V. K. Gusev, N. N. Bakharev, V. A. Belyakov, B. Y. Ber, E. N. Bondarchuk, *et al.*, "Review of Globus-M spherical tokamak results," *Nuclear Fusion*, vol. 55, no. 10, p. 104016, 2015.

[27] V. B. Minaev, V. K. Gusev, N. V. Sakharov, V. I. Varfolomeev, N. N. Bakharev, *et al.*, "Spherical tokamak Globus-M2 : design , integration , construction," 2017.

[28] K. Hanada, K. Sato, H. Zushi, K. Nakamura, M. Sakamoto, *et al.*, "Steady-state operation scenario and the first experimental result on QUEST," *Plasma and Fusion Research*, vol. 5, pp. 1–6, 2010.

[29] H. Idei, T. Kariya, T. Imai, K. Mishra, T. Onchi, *et al.*, "Fully non-inductive second harmonic electron cyclotron plasma ramp-up in the QUEST spherical tokamak," *Nuclear Fusion*, vol. 57, no. 12, p. 126045, 2017.

[30] R. Majeski, R. E. Bell, D. P. Boyle, R. Kaita, T. Kozub, *et al.*, "Compatibility of lithium plasma-facing surfaces with high edge temperatures in the Lithium Tokamak Experiment," *Physics of Plasmas*, vol. 24, no. 5, p. 056110, 2017.

[31] J. C. Schmitt, T. Abrams, L. R. Baylor, L. Berzak Hopkins, T. Biewer, *et al.*, "Results and future plans of the Lithium Tokamak eXperiment (LTX)," *Journal of Nuclear Materials*, vol. 438, no. SUPPL, pp. S1096–S1099, 2013.

[32] M. Gryaznevich and O. Asunta, "Overview and status of construction of ST40," *Fusion Engineering and Design*, vol. 123, pp. 177–180, 2017.

[33] P. F. Buxton, O. Asunta, M. P. Gryaznevich, D. Lockley, S. McNamara, *et al.*, "On the design and role of passive stabilisation within the ST40 spherical tokamak," *Plasma Physics and Controlled Fusion*, vol. 60, no. 6, p. 064008, 2018.

[34] K. J. Chung, Y. H. An, B. K. Jung, H. Y. Lee, C. Sung, *et al.*, "Design features and commissioning of the versatile experiment spherical torus (VEST) at Seoul National University," *Plasma Science and Technology*, vol. 15, no. 3, pp. 244–251, 2013.

[35] K. J. Chung, Y. H. An, B. K. Jung, H. Y. Lee, J. J. Dang, *et al.*, "Initial plasma start-up using partial solenoid coils in Versatile Experiment Spherical Torus (VEST)," *Fusion Engineering and Design*, vol. 88, no. 6-8, pp. 787–790, 2013.

[36] B. G. Hong, Y. S. Hwang, J. S. Kang, D. W. Lee, H. G. Joo, *et al.*, "Conceptual design study of a superconducting spherical tokamak reactor with a self-consistent system analysis code," *Nuclear Fusion*, vol. 51, no. 11, p. 113013, 2011.

[37] R. J. Akers, A. Bond, R. J. Buttery, P. G. Carolan, G. F. Counsell, *et al.*, "Steady state operation of spherical tokamaks," *Nuclear Fusion*, vol. 40, no. 6, pp. 1223–1244, 2000.

[38] M. P. Gryaznevich and S. E. Sharapov, "Beta-dependence of energetic particle-driven instabilities in spherical tokamaks," *Plasma Physics and Controlled Fusion*, vol. 46, no. 7, 2004.

[39] K. G. McClements, M. P. Gryaznevich, S. E. Sharapov, R. J. Akers, L. C. Apell, *et al.*, "Energetic particle-driven instabilities in the START spherical tokamak Physics of energetic particle-driven instabilities in the START spherical tokamak," *Plasma Physics and Controlled Fusion*, vol. 41, pp. 661–678, 1999.

[40] S. J. Doyle, D. Lopez-Aires, A. Mancini, M. Agredano-Torres, and J. L. Garcia-Sanchez, "Equilibrium Design for the SMART Tokamak," *In Review*, pp. 1–12.

[41] A. Mancini, J. Ayllon-Guerola, S. J. Doyle, M. Agredano-Torres, D. Lopez-Aires, *et al.*, "Mechanical and electromagnetic design of the vacuum vessel of the SMART tokamak," *Fusion Engineering and Design*, vol. 171, p. 112542, 2021.

[42] M. Agredano-Torres, J. L. Garcia-Sanchez, A. Mancini, S. J. Doyle, M. Garcia-Munoz, *et al.*, "Coils and power supplies design for the SMART tokamak," *Fusion Engineering and Design*, vol. 168, p. 112683, 2021.

[43] B. K. Jung, K. J. Chung, Y. H. An, J. S. Kang, and Y. S. Hwang, "Design and commissioning of a TF coil power system using deep-cycle batteries for versatile experiment spherical torus (VEST)," *Fusion Engineering and Design*, vol. 88, no. 9-10, pp. 1597–1600, 2013.

[44] E. Fable, C. Angioni, F. J. Casson, D. Told, A. A. Ivanov, *et al.*, "Novel free-boundary equilibrium and transport solver with theory-based models and its validation against ASDEX Upgrade current ramp scenarios," *Plasma Physics and Controlled Fusion*, vol. 55, no. 12, p. 124028, 2013.

[45] G. V. Pereverzev and P. N. Yushmanov, "ASTRAAutomated System for Transport Analysis in a Tokamak," no. IPP 5/98, p. 147, 2002.

[46] P. F. Buxton and M. P. Gryaznevich, "Merging compression start-up predictions for ST40," *Fusion Engineering and Design*, vol. 123, pp. 551–554, 2017.

[47] L. Kripner, M. Peterka, M. Imr, J. Urban, J. Havl, *et al.*, "Equilibrium Design for the COMPASS-U Tokamak," in *WDS Annual Conference of Doctoral Students*, (Prague), pp. 99–104, MATFYPRESS, 2018.

[48] A. Coutlis, I. Bandyopadhyay, J. B. Lister, P. Vyas, R. Albanese, *et al.*, "Measurement of the open loop plasma equilibrium response in TCV," *Nuclear Fusion*, vol. 39, no. 5, pp. 663–683, 1999.

[49] P. Haynes and R. J. Buttery, "TOPEOL: A User's Guide edition 2.0," tech. rep., UKAEA Fusion, Culham, UK, 1995.

[50] L. L. Lao, H. S. John, R. D. Stambaugh, A. G. Kellman, and W. Pfeiffer, "Reconstruction of current profile parameters and plasma shapes in tokamaks," *Nuclear Fusion*, vol. 25, no. 11, pp. 1611–1622, 1985.

[51] G. Cunningham, "High performance plasma vertical position control system for upgraded MAST," *Fusion Engineering and Design*, vol. 88, no. 12, pp. 3238–3247, 2013.

[52] A. S. Sharma, D. J. Limebeer, I. M. Jaimoukha, and J. B. Lister, "Modeling and control of TCV," *IEEE Transactions on Control Systems Technology*, vol. 13, no. 3, pp. 356–369, 2005.

[53] J. B. Lister, A. Sharma, D. J. Limebeer, Y. Nakamura, J. P. Wainwright, *et al.*, "Plasma equilibrium response modelling and validation on JT-60U," *Nuclear Fusion*, vol. 42, no. 6, pp. 708–724, 2002.

[54] X. Garbet, P. Mantica, F. Ryter, G. Cordey, F. Imbeaux, *et al.*, "Profile stiffness and global confinement," *Plasma Physics and Controlled Fusion*, vol. 46, no. 9, pp. 1351–1373, 2004.

[55] J. E. Menard, M. G. Bell, R. E. Bell, E. D. Fredrickson, D. A. Gates, *et al.*, "β-limiting MHD instabilities in improved-performance NSTX spherical torus plasmas," *Nuclear Fusion*, vol. 43, no. 5, pp. 330–340, 2003.

[56] M. Ono, S. M. Kaye, Y. K. Peng, G. Barnes, W. Blanchard, *et al.*, "Exploration of spherical torus physics in the NSTX device," *Nuclear Fusion*, vol. 40, no. SPEC. ISS. 3, pp. 557–561, 2000.

[57] V. Thompson, G. Voss, I. Katramados, and M. Harte, "MAST Upgrade centre column design and analysis," *Fusion Engineering and Design*, vol. 86, no. 6-8, pp. 1398–1401, 2011.

[58] Y. Mitrishkin, A. A. Prokhorov, P. S. Korenev, and M. I. Patrov, "Plasma magnetic time-varying nonlinear robust control system for the Globus-M/M2 tokamak," *Control Engineering Practice*, vol. 100, no. May, p. 104446, 2020.

[59] J. Lee, S. C. Kim, J. Y. Park, Y. G. Kim, Y. H. An, *et al.*, "Development of equilibrium fitting code using finite element method in versatile experiment spherical torus," *Fusion Engineering and Design*, vol. 131, no. September 2017, pp. 141–149, 2018.

[60] S. C. Kim, J. Lee, J. hun Yang, K. S. Chung, K. J. Chung, *et al.*, "Development of diverted plasma discharge and plan for advanced divertor study in VEST," *Fusion Engineering and Design*, vol. 123, pp. 584–587, 2017.

[61] Y. An, J. Lee, H. Lee, J. Jo, B. K. Jung, *et al.*, "Plasma start-up design and first plasma experiment in VEST," *Fusion Engineering and Design*, vol. 96-97, pp. 274–280, 2015.

[62] O. Mitarai, K. Nakamura, S. Tashima, M. Hasegawa, H. Idei, *et al.*, "First ohmic discharge assisted with RF power in QUEST spherical tokamak," *Plasma and Fusion Research*, vol. 6, no. 2011, pp. 1–9, 2011.